Bull. Chem. Soc. Ethiop. **2024**, 38(6), 1775-1790.
DOI: https://dx.doi.org/10.4314/bcse.v38i6.21

ISSN 1011-3924
Printed in Ethiopia
Online ISSN 1726-801X

THEORETICAL INVESTIGATION OF NORFLOXACIN HYBRID COMPOUNDS WITH SILVER, COPPER, AND GOLD METALS AS POTENTIAL ANTICANCER AGENTS

Amnah Mohammed Alsuhaibani[1], Sonam Shakya[2], Maidul Islam[2,3] and Moamen S. Refat[4*]

[1]Department of Physical Sport Science, College of Sport Sciences & Physical Activity, Princess Nourah bint Abdulrahman University, P.O. Box 84428, Riyadh 11671, Saudi Arabia
[2]Department of Chemistry, Faculty of Science, Aligarh Muslim University, Aligarh 202002, India
[3]Research and Development Cell, Lovely Professional University, Phagwara, Punjab-144411, India
[4]Department of Chemistry, College of Science, Taif University, P.O. Box 11099, Taif 21944, Saudi Arabia

(Received June 30, 2024; Revised July 28, 2024; Accepted August 1, 2024)

ABSTRACT. The strategy of drug repurposing and repositioning in developing hybrid molecules is significant in drug discovery. Norfloxacin (Nor) hybrids, part of the fluoroquinolone class of antibiotics, have demonstrated anticancer properties. Various norfloxacin metal complexes have been synthesized and evaluated for their anticancer potential through docking simulations using AutoDock Vina. To preliminarily identify potential molecular targets for these anticancer compounds, docking studies were conducted with a variety of enzymes and receptor proteins associated with the cell cycle, cell growth, and DNA replication. These targets included cyclin dependent protein kinase-2 (CDK-2), CDK-6, DNA topoisomerases I and II, B cell lymphoma-2 (Bcl-2), and vascular endothelial growth factor receptor-2 (VEGFR-2). Density functional theory (DFT) and time-dependent density functional theory (TD-DFT) calculations were conducted utilizing the B3LYP functional with the 6-311G++ and LanL2DZ basis sets. This study investigated the optimized geometries, molecular electrostatic potential (MEP) maps, key molecular properties, and HOMO-LUMO energy gaps of Nor, Nor zwitterionic structure, and its synthesized compounds ($[Ag_2(Nor)_2](NO_3)_2$, $[Cu(Nor)_2(H2O)_2]SO_4.5H_2O$, and $[Au(Nor)_2(H_2O)_2]Cl_3$).

KEY WORDS: Norfloxacin, Anticancer agents, DFT/ TD-DFT, Molecular docking

INTRODUCTION

Norfloxacin (Nor) hybrid compounds, a well-known class of antibiotics, have been explored by combining them with other pharmacophores to evaluate their anticancer activity both in silico and in vitro. Recent studies have focused on Nor's structure-activity relationships and potential strategies for developing potent chemotherapeutic agents. In this study, compounds synthesized using Nor were examined using the AutoDock Vina program to identify potential molecular targets and support tests of enzyme and receptor protein anticancer activity [1]. Docking simulations were conducted to assess interactions with six different molecular targets associated with the cell cycle, cell growth, and DNA replication: cyclin dependent protein kinase-2 (CDK-2), cyclin-dependent protein kinase-6 (CDK-6), DNA topoisomerase I, DNA topoisomerase II, B cell lymphoma-2 (Bcl-2), and vascular endothelial growth factor receptor-2 (VEGFR-2). These simulations provided preliminary insights into the potential efficacy of the synthesized Nor hybrid compounds as anticancer agents [2].

Cyclin-dependent kinases 2 and 6 (CDK-2 and CDK-6) are Ser/Thr kinases that play crucial roles in regulating the cell cycle, apoptosis, transcription, and neuronal functions. These kinases become active only when associated with regulatory partners, such as cyclins or other proteins [3,

*Corresponding authors. E-mail: moamen@tu.edu.sa; msrefat@yahoo.com

4]. DNA topoisomerases I and II are essential enzymes for cell survival, involved in critical aspects of DNA metabolism and structural maintenance. Topoisomerase I alleviates DNA superhelical tension by cleaving one strand of duplex DNA and unwinding supercoiled DNA. In contrast, topoisomerase II induces transient breaks in both DNA strands, facilitating necessary topological transformations [5, 6]. B cell lymphoma-2 (Bcl-2) is a protein that plays a pivotal role in the regulation of apoptosis. Apoptosis is a crucial process for maintaining cellular homeostasis by eliminating aged or damaged cells and accommodating the billions of new cells produced daily. The Bcl-2 protein family includes both pro-apoptotic and anti-apoptotic members, which have opposing functions in promoting or inhibiting cell death. Elevated levels of Bcl-2 are commonly associated with various human cancers, underscoring its significance in oncogenesis [7]. Vascular endothelial growth factor receptor-2 (VEGFR-2) is a cell surface receptor specific for VEGF, a potent mitogen for vascular endothelial cells. VEGFR-2 is expressed primarily in endothelial cells and plays a key role in angiogenesis, the formation of new blood vessels, and tumor growth. Its involvement in these processes makes it a critical target for anti-cancer therapies aimed at inhibiting tumor vascularization and progression [8].

Using molecular docking with AutoDock Vina software, we analyzed and compared the binding affinities and interactions of Nor and its synthesized compounds ($[Ag_2(Nor)_2](NO_3)_2$, $[Cu(Nor)_2(H2O)_2]SO_4.5H_2O$, and $[Au(Nor)_2(H_2O)_2]Cl_3$) with six key receptors: CDK-2, CDK-6, DNA topoisomerases I and DNA topoisomerases II, Bcl-2, and VEGFR-2. Our analysis focused on several crucial parameters, including binding energy, interpolated charge, solvent-accessible surface area (SAS), ionizability, hydrophobic interactions, hydrogen bonding, and aromatic interactions at the binding sites. By evaluating these parameters, we comprehensively understood the molecular interactions between the compounds and the target receptors. This in-depth analysis provided insights into the potential therapeutic efficacy of these Nor-based compounds, shedding light on their possible roles as anticancer agents. We conducted computational calculations using density functional theory (DFT) and time-dependent density functional theory (TD-DFT) at the B3LYP/6-311G++ and LanL2DZ levels of theory [9]. This comprehensive study included the analysis of optimized geometries, molecular electrostatic potential maps, and the electronic energy gaps between the highest occupied molecular orbital (HOMO) and the lowest unoccupied molecular orbital (LUMO) for Nor and its synthesized compounds ($[Ag_2(Nor)_2](NO_3)_2$, $[Cu(Nor)_2(H_2O)_2]SO_4.5H_2O$, and $[Au(Nor)_2(H_2O)_2]Cl_3$). Furthermore, we thoroughly investigated additional key parameters, such as structural, chemical, and spectroscopic properties, to provide a holistic understanding of these compounds. The optimized geometries revealed the spatial arrangement of atoms, while the molecular electrostatic potential maps highlighted regions of electron density, crucial for predicting reactivity and interaction sites. The HOMO-LUMO energy gaps provided insights into the electronic stability and reactivity of the molecules [10-14].

EXPERIMENTAL

Molecular docking simulation

The initial molecular structures of Nor and its synthesized compounds ($[Ag_2(Nor)_2](NO_3)_2$, $[Cu(Nor)_2(H_2O)_2]SO_4.5H_2O$, and $[Au(Nor)_2(H_2O)_2]Cl_3$) were optimized using density functional theory (DFT) calculations, which provided the foundational geometries for our study. These optimized structures were converted to PDBQT format utilizing OpenBabelIGUI software version 2.4.1 [15, 16], accessible at http://openbabel.org/wiki/Main_Page. Structural data for the target receptors - CDK-2 (PDB ID: 1DI8), CDK-6 (PDB ID: 1XO2), Topoisomerase I (PDB ID: 1T8I), Topoisomerase II (PDB ID: 1ZXM), Bcl-2 (PDB ID: 2O2F), and VEGFR-2 (PDB ID: 2OH4) - were sourced from the RCSB Protein Data Bank [17].

Receptor structures were prepared for docking by removing native ligands and other heteroatoms, including water molecules, using BIOVIA Discovery Studio Visualizer

(v19.1.0.18287). To ensure accurate docking, polar hydrogen atoms were added, and Kollman charges were assigned via Autodock Tools [18], with partial charges calculated using the Gasteiger method. The docking simulations of Nor and its compounds with the receptors were conducted using AutoDock Vina [19]. The resulting docked poses were thoroughly analyzed to assess interactions, with detailed scrutiny performed using Discovery Studio (DS) Visualizer (https://www.3ds.com/products-services/biovia/). The computational work was executed on a computer equipped with an Intel(R) Core(TM) i5-4200U CPU @ 1.60 GHz, 2.10 GHz, 2.30 GHz, 64-bit architecture. This meticulous computational approach allowed us to gain significant insights into the binding interactions and potential efficacy of Nor and its compounds as therapeutic agents. Detailed analysis of the docking poses provided valuable information on the molecular interactions at the binding sites of the target receptors [20], shedding light on the therapeutic potential and mechanistic pathways of these compounds.

Density functional theory (DFT) and time-dependent density functional theory (TD-DFT)

We utilized the Gaussian 09RevD.01 software package [21] for our density functional theory (DFT) calculations. These calculations were designed to achieve optimized molecular geometries and examine electronic transitions in Nor and its synthesized compounds ($[Ag_2(Nor)_2](NO_3)_2$, $[Cu(Nor)_2(H_2O)_2]SO_4.5H_2O$, and $[Au(Nor)_2(H_2O)_2]Cl_3$). The geometry optimization was conducted using the B3LYP functional combined with the 6-311G++ basis set for non-metal atoms. For Ag, Cu, and Au atoms, we employed the Los Alamos Effective Core Potentials (LanL2DZ) basis set [22]. This combination of functionals and basis sets enabled precise modeling of both organic and inorganic components within the compounds. Our study extended to several key molecular properties, including the generation of molecular electrostatic potential (MEP) maps and the analysis of frontier molecular orbitals (FMOs), particularly the highest occupied molecular orbital (HOMO) and the lowest unoccupied molecular orbital (LUMO). These properties were essential for evaluating the electronic characteristics and chemical stability of Nor and its synthesized compounds [23]. The MEP maps provided insights into the charge distribution within the molecules, while the HOMO-LUMO analysis helped us understand the electronic transitions and reactivity patterns.

Additionally, we calculated the infrared (IR) frequencies, all of which were positive, confirming that the optimized geometries correspond to minima on the potential energy surface. By examining the vibrational modes, we were able to accurately assign the bands observed in the Fourier-transform infrared (FT-IR) spectra of both the parent compound and its synthesized derivatives. Our theoretical investigation extended to the analysis of structure-based molecular properties in the gas phase, employing the same computational methods. This allowed us to explore various electronic and structural parameters crucial for understanding the compounds' behavior and reactivity. For the visualization of molecular structures and properties, we utilized ChemCraft 1.5 software [24], which provided clear and detailed representations of the molecules and their electronic characteristics.

RESULTS AND DISCUSSION

Molecular docking simulation studies

We conducted comprehensive molecular docking studies to investigate the interactions between Nor and its synthesized compounds ($[Ag_2(Nor)_2](NO_3)_2$, $[Cu(Nor)_2(H_2O)_2]SO_4.5H_2O$, and $[Au(Nor)_2(H_2O)_2]Cl_3$) as anticancer drug with six different enzymes and receptor proteins involved with cell cycle, cell growth, and DNA replication: CDK-2 (PDB ID: 1DI8), CDK-6 (PDB ID: 1XO2), Topoisomerase I (PDB ID: 1T8I), Topoisomerase II (PDB ID: 1ZXM), Bcl-2 (PDB ID: 2O2F), and VEGFR-2 (PDB ID: 2OH4). Our goal was to identify the most favorable

docking poses and evaluate the relative binding efficiencies of Nor and its synthesized compounds. The results of our docking studies revealed significant insights into the binding affinities of these compounds. The $[Au(Nor)_2(H_2O)_2]Cl_3$ compound demonstrated a higher potential binding energy compared to Nor and the other synthesized compounds for all receptors. Specifically, the $[Au(Nor)_2(H_2O)_2]Cl_3$ compound exhibited the highest docking energy value when interacting with the topoisomerase II (PDB ID: 1ZXM), with a potential binding energy of -13.9 kcal/mol. This indicates a stronger interaction between the $[Au(Nor)_2(H_2O)_2]Cl_3$ compound and Topoisomerase II compared to the other complexes [25]. Table 1 presents a detailed comparison of the docking data, including the potential binding energies for Nor and its synthesized compounds with all six receptors. The most favorable docking poses for Nor and $[Au(Nor)_2(H_2O)_2]Cl_3$ compound with different receptors are illustrated in Figure 1. Additionally, the molecular docking interactions are depicted in both 3D and 2D representations for topoisomerase II (PDB ID: 1ZXM) with Nor, $[Ag_2(Nor)_2](NO_3)_2$, $[Cu(Nor)_2(H_2O)_2]SO_4.5H_2O$, and $[Au(Nor)_2(H_2O)_2]Cl_3$ compound, is represented in Figure 2. These findings highlight the superior binding affinity of $[Au(Nor)_2(H_2O)_2]Cl_3$ compound, suggesting its potential as a more effective therapeutic agent for conditions related to these receptors. Our comprehensive docking analysis provides valuable insights into the molecular interactions and stability of these compounds, paving the way for further experimental validation and potential pharmaceutical applications [26, 27].

Table 1. The interactions of Nor and synthesized compounds docked with different enzymes and receptor proteins involved with cell cycle, cell growth, and DNA replication.

Target macromolecule	PDB code	Ligand	Binding free energy (kcal/mol)
CDK-2	1DI8	Nor	-8.7
		$[Ag_2(Nor)_2](NO_3)_2$	-10.3
		$[Cu(Nor)_2(H2O)_2]SO_4.5H_2O$	-8.5
		$[Au(Nor)_2(H_2O)_2]Cl_3$	-11.4
CDK-6	1XO2	Nor	-8.4
		$[Ag_2(Nor)_2](NO_3)_2$	-9.5
		$[Cu(Nor)_2(H2O)_2]SO_4.5H_2O$	-8.9
		$[Au(Nor)_2(H_2O)_2]Cl_3$	-10.7
Topoisomerase I	1T8I	Nor	-8.6
		$[Ag_2(Nor)_2](NO_3)_2$	-11.4
		$[Cu(Nor)_2(H2O)_2]SO_4.5H_2O$	-11.2
		$[Au(Nor)_2(H_2O)_2]Cl_3$	-11.9
Topoisomerase II	1ZXM	Nor	-9.1
		$[Ag_2(Nor)_2](NO_3)_2$	-10.3
		$[Cu(Nor)_2(H2O)_2]SO_4.5H_2O$	-8.4
		$[Au(Nor)_2(H_2O)_2]Cl_3$	-13.9
Bcl-2	2O2F	Nor	-6.7
		$[Ag_2(Nor)_2](NO_3)_2$	-9.9
		$[Cu(Nor)_2(H2O)_2]SO_4.5H_2O$	-7.8
		$[Au(Nor)_2(H_2O)_2]Cl_3$	-10.3
VEGFR-2	2OH4	Nor	-8.0
		$[Ag_2(Nor)_2](NO_3)_2$	-10.4
		$[Cu(Nor)_2(H2O)_2]SO_4.5H_2O$	-8.4
		$[Au(Nor)_2(H_2O)_2]Cl_3$	-11.8

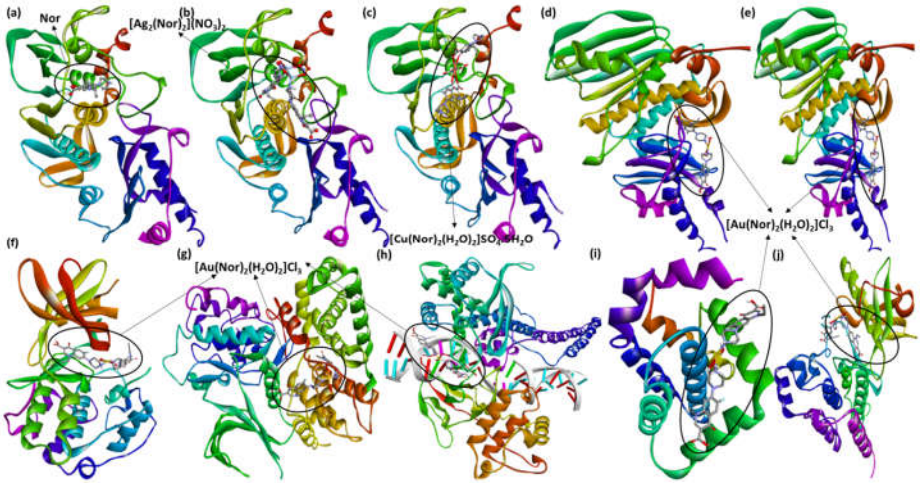

Figure 1. Best docked pose showing a helical model of (a,b,c,d) topoisomerase II (PDB ID: 1ZXM) docked with Nor, $[Ag_2(Nor)_2](NO_3)_2$, $[Cu(Nor)_2(H_2O)_2]SO_4.5H_2O$, and $[Au(Nor)_2(H_2O)_2]Cl_3$ compound, respectively, and (e, f, g, h, i) $[Au(Nor)_2(H_2O)_2]Cl_3$ compound docked with CDK-2 (PDB ID: 1DI8), CDK-6 (PDB ID: 1XO2), topoisomerase I (PDB ID: 1T8I), Bcl-2 (PDB ID: 2O2F), and VEGFR-2 (PDB ID: 2OH4), respectively.

As shown in Figure 2, Nor with topoisomerase II reveals the amino acid residues, including Arg98 and Asn120, forming hydrogen bond interactions. Additionally, Asn95, Thr147, and Asn91 form carbon-hydrogen bond; Asn91 forms halogen (fluorine) bond; Arg98 forms alkyl bond; and Ile125 with π-Alkyl bond, are also present [28]. On the other hand $[Au(Nor)_2(H_2O)_2]Cl_3$ compound with topoisomerase II for hydrogen bond with Lys83, Arg241, Lys357, Phe308, Trp62, Glu379, Gln60, Lys321, Tyr82, and Met61. Also, Ala318 and Met61, including carbon-hydrogen, form hydrophobic bonds (Figure 2). These findings suggest that the synthesized $[Au(Nor)_2(H_2O)_2]Cl_3$ compound exhibits more efficient binding with topoisomerase II along with other receptors also. Table 2 presents a detailed comparison of the docking data, including the potential binding energies obtained from Discovery Studio (DS) software.

Surface interaction study by discovery studio (DS) software

We conducted an in-depth analysis of the molecular docking results using discovery studio (DS) software, which offered advanced visualization tools to examine the interaction surfaces between the ligands and receptor binding sites. This sophisticated software enabled us to create detailed graphical representations of the interaction sites, highlighting various physicochemical properties [29]. Figure 3 presents a series of graphical illustrations that emphasize the key interaction features at the binding sites. These features include hydrogen bonding, interpolated charge, aromatic interactions, hydrophobic interactions, ionizability, and solvent-accessible surface (SAS) areas. This comprehensive visualization not only enhances our understanding of the binding interactions but also provides valuable insights into the molecular mechanisms underlying the potential therapeutic efficacy of the compounds.

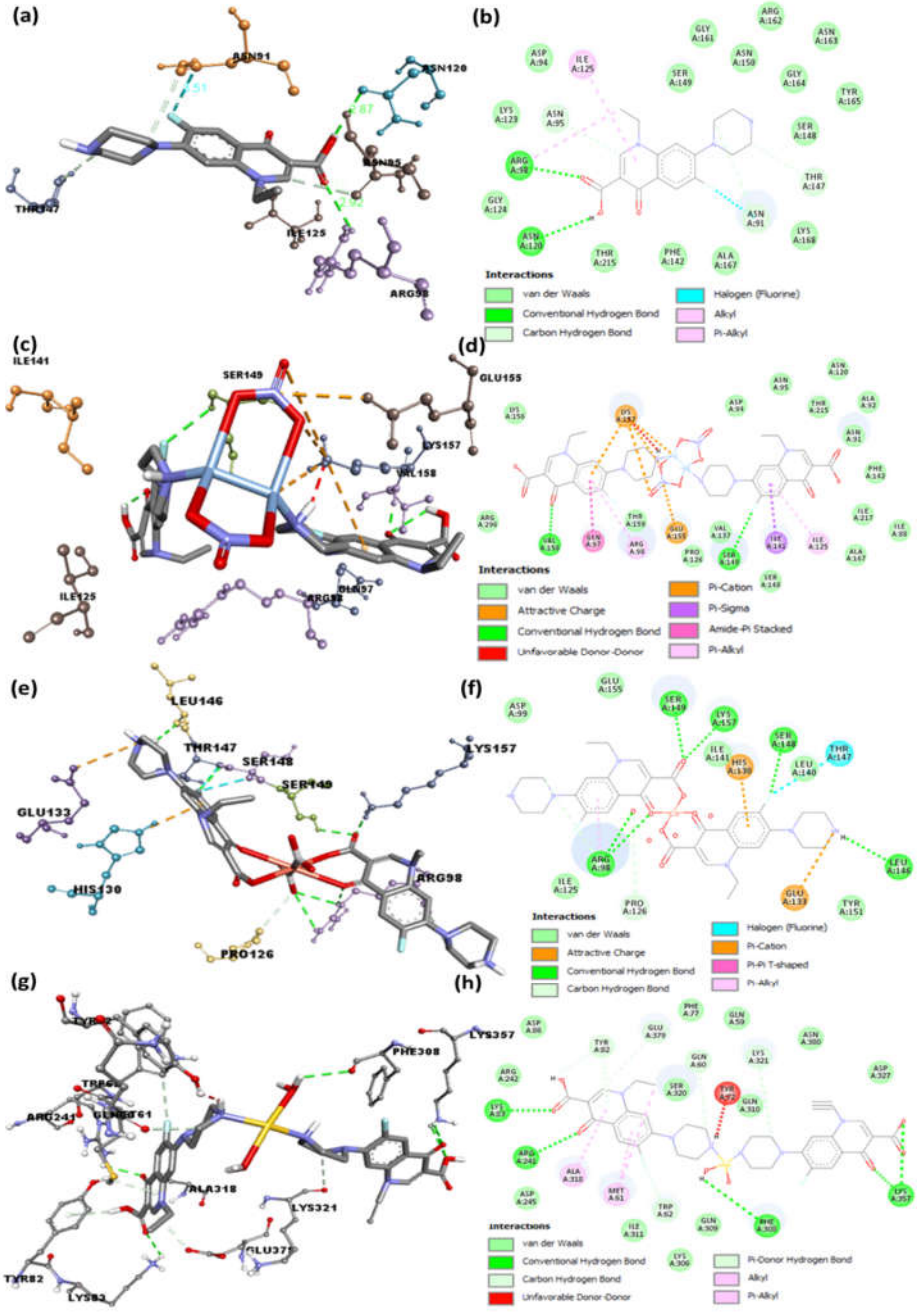

Figure 2. 3D and 2D representation of interactions between topoisomerase II (PDB ID: 1ZXM) with (a, b) Nor, (c, d) $[Ag_2(Nor)_2](NO_3)_2$, (e, f) $[Cu(Nor)_2(H_2O)_2]SO_4.5H_2O$, and (g, h) $[Au(Nor)_2(H_2O)_2]Cl_3$ compound, respectively.

Table 2. Nor and $[Au(Nor)_2(H_2O)_2]Cl_3$ compound interaction results with topoisomerase II (PDB ID: 1ZXM) by DS.

Name	Distance	Category	Type
ARG98:H12 - Nor:O	2.91817	Hydrogen Bond	Conventional Hydrogen Bond
Nor:H - ASN120:OD1	2.86759	Hydrogen Bond	Conventional Hydrogen Bond
Nor:C - ASN95:OD1	3.1803	Hydrogen Bond	Carbon Hydrogen Bond
Nor:C - THR147:O	3.25117	Hydrogen Bond	Carbon Hydrogen Bond
Nor:C - ASN91:OD1	3.51839	Hydrogen Bond	Carbon Hydrogen Bond
ASN91:CG - Nor:F	3.50985	Halogen	Halogen (Fluorine)
Nor:C - ARG98	4.24591	Hydrophobic	Alkyl
Nor - ILE125	5.23197	Hydrophobic	Pi-Alkyl
LYS83:HZ1 - $[Au(Nor)_2(H_2O)_2]Cl_3$:O	2.63461	Hydrogen Bond	Conventional Hydrogen Bond
ARG241:HH22 - $[Au(Nor)_2(H_2O)_2]Cl_3$:O	2.52626	Hydrogen Bond	Conventional Hydrogen Bond
LYS357:HZ1 - $[Au(Nor)_2(H_2O)_2]Cl_3$:O	2.92503	Hydrogen Bond	Conventional Hydrogen Bond
LYS357:HZ2 - $[Au(Nor)_2(H_2O)_2]Cl_3$:O	2.4713	Hydrogen Bond	Conventional Hydrogen Bond
LYS357:HZ2 - $[Au(Nor)_2(H_2O)_2]Cl_3$:O	2.95701	Hydrogen Bond	Conventional Hydrogen Bond
$[Au(Nor)_2(H_2O)_2]Cl_3$:H50 - PHE308:O	3.06402	Hydrogen Bond	Conventional Hydrogen Bond
TRP62:CD1 - $[Au(Nor)_2(H_2O)_2]Cl_3$:F	3.52331	Hydrogen Bond	Carbon Hydrogen Bond
$[Au(Nor)_2(H_2O)_2]Cl_3$:C - GLU379:OE2	3.41437	Hydrogen Bond	Carbon Hydrogen Bond
$[Au(Nor)_2(H_2O)_2]Cl_3$:C - GLN60:O	3.35415	Hydrogen Bond	Carbon Hydrogen Bond
$[Au(Nor)_2(H_2O)_2]Cl_3$:C - LYS321:O	3.7282	Hydrogen Bond	Carbon Hydrogen Bond
TYR82:HH - $[Au(Nor)_2(H_2O)_2]Cl_3$	3.2342	Hydrogen Bond	Pi-Donor Hydrogen Bond
$[Au(Nor)_2(H_2O)_2]Cl_3$:H - TYR82	2.97338	Hydrogen Bond	Pi-Donor Hydrogen Bond
$[Au(Nor)_2(H_2O)_2]Cl_3$:C - MET61	5.18593	Hydrophobic	Alkyl
$[Au(Nor)_2(H_2O)_2]Cl_3$ - ALA318	5.13864	Hydrophobic	Pi-Alkyl
$[Au(Nor)_2(H_2O)_2]Cl_3$ - MET61	4.61574	Hydrophobic	Pi-Alkyl

In this study, we employed hydrogen bond surface figures to visually represent the complex hydrogen bonding interactions within a molecular framework, as illustrated in Figure 3a. This graphical depiction utilizes a color-coded scheme to highlight the amino acid residues involved in hydrogen bonding interactions, with hydrogen atom acceptor sites shown in green and donor sites depicted in pink. The connections between these sites are represented by lines or dashed lines, which delineate the hydrogen bonds and visually distinguish the donor and acceptor roles through color differentiation. This detailed graphical representation effectively captures the hydrogen bond topology, providing a clear and informative visualization of the specific amino acid residues participating in these critical interactions. By emphasizing the spatial arrangement and interactions of the hydrogen bonds, this figure offers valuable insights into the molecular recognition and binding mechanisms at play. Interpolated charge calculation involves determining the partial atomic charges distributed throughout a molecule, thereby enhancing the accuracy of molecular modeling [30]. This methodological approach is crucial for predicting electrostatic interactions, which are key to understanding binding affinities. It also aids in refining drug design strategies by providing a detailed analysis of molecular properties and interactions (see Figure 3b). The visualization of the aromatic face and edge surfaces, shown in orange and blue respectively in Figure 3c, offers valuable insights into their spatial arrangement and electrostatic properties. This detailed depiction enhances our understanding of molecular interactions by highlighting the specific areas where these interactions occur [31]. Hydrophobicity surface figures, as depicted in Figure 3d, provide a visual representation of the hydrophobic regions within a molecular framework. Typically, hydrophobic areas are shown in varying shades of blue, while hydrophilic regions are rendered in neutral or contrasting colors. These visualizations elucidate the interaction dynamics between molecules and water, highlighting how hydrophobic regions repel aqueous environments. The analysis of hydrophobicity surfaces confirms the presence of complementary hydrophilic interactions at the receptor-ligand interface by identifying

hydrophilic features surrounding the ligand. This approach offers a deeper understanding of the molecular interactions at play. Ionization surface figures, shown in Figure 3e, visually illustrate the acidic and basic characteristics of a molecular surface. In this graphical representation, regions with basic properties are highlighted in shades of blue, while those with acidic tendencies are depicted in hues of red. These visualizations are valuable for understanding the electrostatic profile of molecular surfaces, providing insights into charge-based interactions [32]. Solvent accessible surface (SAS) figures, depicted in Figure 3f, visually represent the surface area of a receptor that is accessible to solvent molecules, which is a critical parameter for understanding molecular interactions. In this visualization, areas with limited solvent accessibility are depicted in green, indicating regions less susceptible to solvent penetration. Conversely, regions with higher accessibility are highlighted in blue, particularly emphasizing polar regions. This graphical representation aids in identifying molecular sites that are likely to interact with the surrounding solvent environment, thereby enhancing our understanding of solvation effects [33].

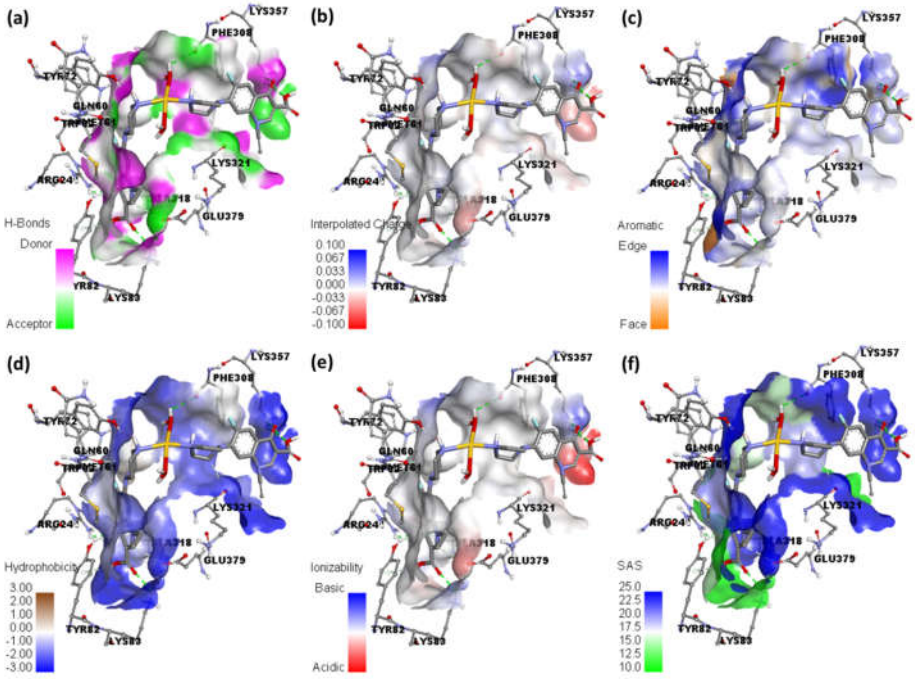

Figure 3. Representation of **(a)** hydrogen binding surface, **(b)** Interpolated charge, **(c)** aromatic surface, **(d)** hydrophobic surface, **(e)** ionizability surface, and **(f)** solvent accessible surface; between topoisomerase II (PDB ID: 1ZXM) and $[Au(Nor)_2(H_2O)_2]Cl_3$ compound.

Density functional theory & time- dependent density functional theory calculations

We employed the B3LYP functional combined with the 6-311G++ and LanL2DZ basis sets to achieve optimized structures for Nor, Nor zwitterionic structure, and synthesized compounds ($[Ag_2(Nor)_2](NO_3)_2$, $[Cu(Nor)_2(H_2O)_2]SO_4.5H_2O$, and $[Au(Nor)_2(H_2O)_2]Cl_3$). The Self-Consistent Field (SCF) energy calculations revealed that the minimum energy for Nor was -1095.950355

atomic units (a.u.) and for $[Au(Nor)_2(H_2O)_2]Cl_3$) compound it is -2478.067987 a.u. The optimized geometries, detailed atomic coordinates, and strain-free lattice constants can be seen in Figure 4. These optimized parameters provide a robust foundation for subsequent analyses, ensuring the accuracy and reliability of our computational results. This meticulous optimization process is critical for understanding these complexes' electronic structure and potential reactivity. The electrostatic potential strengths for Nor, Nor zwitterionic structure, and $[Au(Nor)_2(H_2O)_2]Cl_3$) compound are illustrated in the molecular electrostatic potential (MEP) maps, shown in Figure 5. These maps use a color scale where electropositive regions are represented in blue and electronegative regions in red, highlighting the preferential binding sites for electrophilic and nucleophilic interactions on the molecules [34]. The MEP surface maps are presented on a color scale ranging from deep red to deep blue, corresponding to the following ranges: -7.731e-2 to +7.731e-2 for Nor, -6.612e-2 to +6.612e-2 for Nor zwitterionic structure, and -7.907-2 to +7.907e-2 for $[Au(Nor)_2(H_2O)_2]Cl_3$) compound. These ranges provide a clear visualization of the electrostatic potential distribution and indicate the reactive sites for potential interactions, as shown in Figure 5. By analyzing these MEP maps, we can identify the regions on each molecule that are most likely to engage in electrophilic or nucleophilic interactions, providing insights into their chemical behavior and potential applications [35].

We conducted an in-depth investigation of the infrared spectra of Nor and $[Au(Nor)_2(H_2O)_2]Cl_3$) compound in the gas phase using density functional theory (DFT) at the B3LYP/LanL2DZ level of theory. This computational approach was employed to complement and corroborate experimental findings. The simulated IR spectra were scaled by a factor of 0.90121, as illustrated in Figure 6. Several key vibrational signals observed in the experimental FTIR spectra were found to align well with those in the simulated infrared spectra. This correlation was confirmed by analyzing the animated vibrational modes [36]. It is important to note that some deviations between the simulated and experimental data are anticipated due to the inherent simplifications and anharmonicity within the basis set used in the DFT calculations. Consequently, a scaling factor was applied to the simulated vibrational frequencies to achieve better agreement with the experimental results. These findings demonstrate that the DFT-based simulated spectra effectively replicate the experimental observations, thereby validating the theoretical model and providing deeper insights into the vibrational characteristics of Nor and $[Au(Nor)_2(H_2O)_2]Cl_3$) compound [37]. Deviations between simulated and experimental data in DFT calculations arise from inherent simplifications and anharmonicity within the basis set. DFT models use approximations, such as specific functionals and basis sets, that may not fully capture real molecular behaviors. Additionally, DFT assumes harmonic oscillations, while real molecular vibrations are anharmonic, deviating from the quadratic potential energy surface, especially at higher energy levels. Basis sets like B3LYP/LanL2DZ may not account for all electron correlation effects, causing discrepancies. These factors necessitate scaling factors to improve agreement and validate the computational models against experimental results.

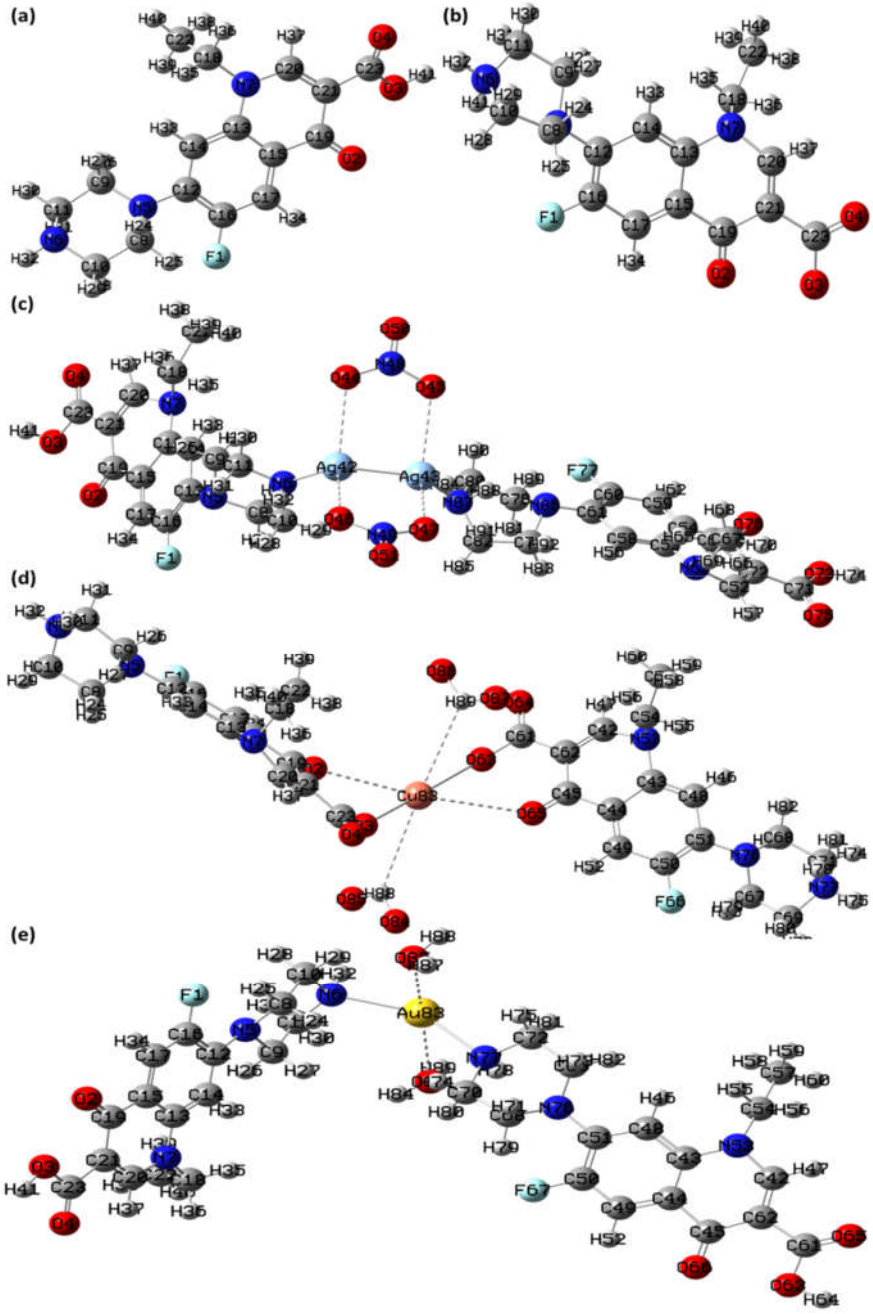

Figure 4. Optimized structure of (a) Nor, (b) Nor zwitterionic structure, (c) $[Ag_2(Nor)_2](NO_3)_2$, (d) $[Cu(Nor)_2(H2O)_2]SO_4.5H_2O$, and (e) $[Au(Nor)_2(H_2O)_2]Cl_3$ compound with Mulliken atom numbering scheme.

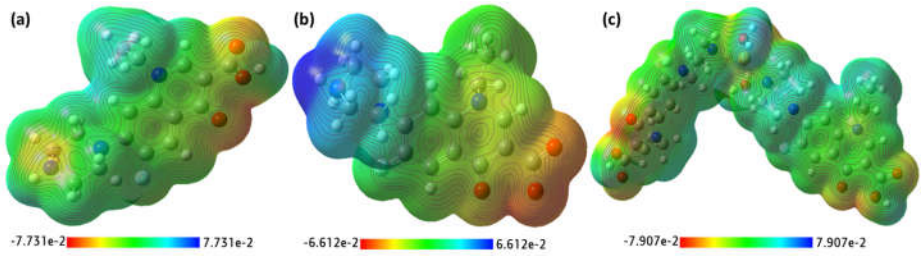

Figure 5. MEP surface map obtained from optimized structure of (a) Nor, (b) Nor zwitterionic structure, and (c) $[Au(Nor)_2(H_2O)_2]Cl_3$ compound with respective color scales.

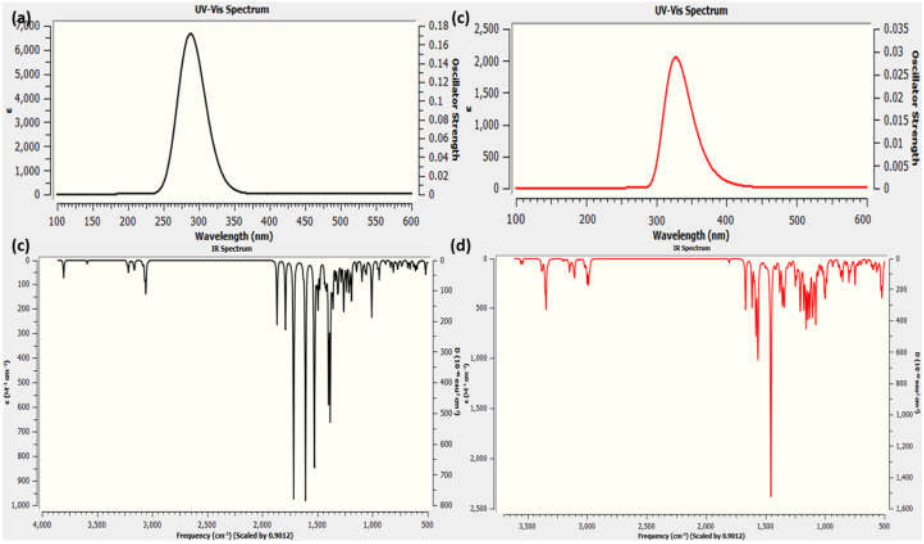

Figure 6. Theoretical UV spectra of (a) Nor and (b) $[Au(Nor)_2(H_2O)_2]Cl_3$ compound obtained through TD-DFT calculations; and simulated (DFT) IR spectra of (a) Nor and (b) $[Au(Nor)_2(H_2O)_2]Cl_3$ compound.

We investigated the electronic transitions of Nor and $[Au(Nor)_2(H_2O)_2]Cl_3$) compound in the gas phase using Time-Dependent Density Functional Theory (TD-DFT). The TD-DFT calculations revealed maximum absorption bands at wavelengths of 288 nm for Nor and 312 nm for $[Au(Nor)_2(H_2O)_2]Cl_3$) compound [38]. These results are presented in Figure 6, which also illustrates the spatial arrangements of the Highest Occupied Molecular Orbital (HOMO) and the Lowest Unoccupied Molecular Orbital (LUMO), as well as the HOMO-LUMO energy gaps for each compound. The HOMO-LUMO energy gap (ΔE) was found to be 4.5185 eV for Nor and 3.9738 eV for $[Au(Nor)_2(H_2O)_2]Cl_3$) compound (Figure 7). The HOMO-LUMO energy gap for Nor is larger compared to $[Au(Nor)_2(H_2O)_2]Cl_3$). This difference can be attributed to the interaction between Nor and the Au ions in the $[Au(Nor)_2(H_2O)_2]Cl_3$) complex. The coordination with Au ions affects the electronic structure, reducing the HOMO-LUMO gap by stabilizing the HOMO or destabilizing the LUMO. The smaller energy gap in $[Au(Nor)_2(H_2O)_2]Cl_3$) indicates higher chemical reactivity and lower kinetic stability compared to Nor alone [39]. These energy

gaps provide insights into the chemical stability of the molecules, with smaller energy gaps indicating higher chemical reactivity, lower kinetic stability, and a softer nature. Conversely, larger energy gaps suggest higher stability and lower reactivity. Table 3 provides a summary of various molecular parameters derived from the gas-phase analysis, including HOMO-LUMO properties and optimized geometries. These comprehensive data underscore the significant electronic characteristics and stability profiles of Nor and its synthesized compounds, contributing valuable insights into their potential applications and reactivity profiles [40, 41].

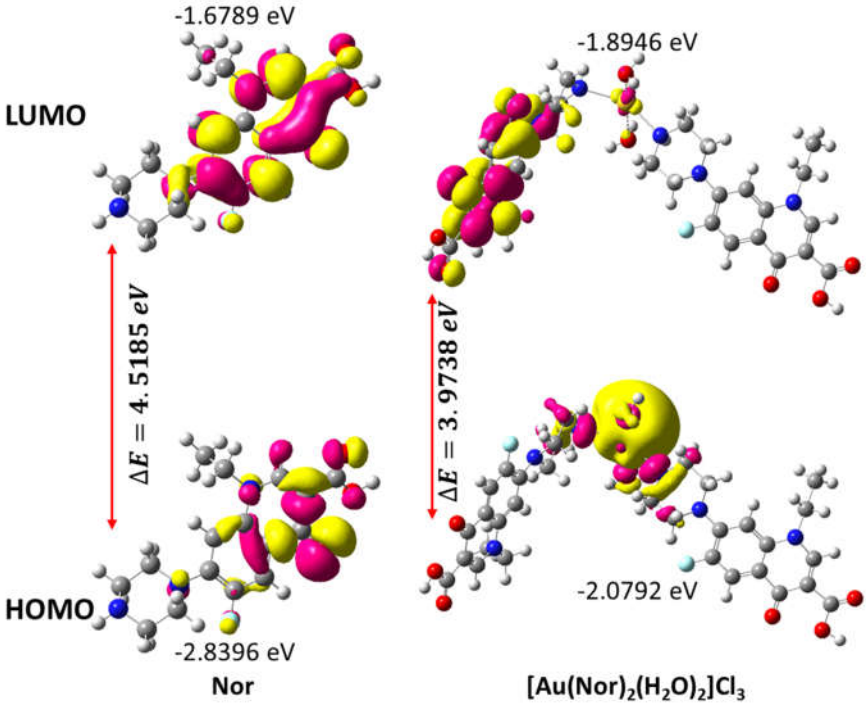

Figure 7. Spatial plot of HOMO and LUMO with their energy gap for Nor and $[Au(Nor)_2(H_2O)_2]Cl_3$ compound.

Table 3. Various other theoretical molecular parameters of Nor and $[Au(Nor)_2(H_2O)_2]Cl_3$ compound.

Parameters	RB3LYP/ lanL2DZ	
	Vit B13	$[Au(Nor)_2(H_2O)_2]Cl_3$ Compound
Minimum SCF energy (a.u.)	-1095.950355	-2478.067987
Polarizability (α) (a.u.)	134.315291	384.696101
Dipole Moment (Debye)	5.028040	3.226040
Zero point vibrational energy (kcal/mol)	221.47047	467.29381
Total thermal energy (kcal/mol)	230.349	496.455
Electronic spatial extent (a.u.)	9301.8049	72603.1975
Frontier MO energies (eV)		
LUMO	-1.6789	-1.8946
HOMO	-2.8396	-2.9738
Gap (HOMO – LUMO)	4.5185	3.8866

CONCLUSION

We used molecular docking simulations to identify potential molecular targets for synthesized norfloxacin (Nor) compounds with reported anticancer activity. Analyzing the best-docked ligands elucidated their binding modes, confirming their role as anticancer agents. Our molecular docking studies demonstrated that the synthesized compound $[Au(Nor)_2(H_2O)_2]Cl_3$) exhibits enhanced interaction efficiency with all six enzymes and receptor proteins involved in cell cycle regulation, cell growth, and DNA replication associated with human cancer. Particularly noteworthy was its high affinity for topoisomerase II, which plays a crucial role in DNA metabolism by inducing transient breaks in both DNA strands. This strong interaction highlights the compound's potential therapeutic efficacy in cancer treatment. The results obtained from our study provide insights into structural features that enhance inhibitory activity against cancer targets. Additionally, Density Functional Theory (DFT) calculations were crucial in elucidating the molecular geometry of the compounds. Examination of the band gap energies of Nor and its derivatives revealed significant trends in stability, providing valuable insights that can inform future research directions in this field.

ACKNOWLEDGMENT

The authors extend their appreciation to Taif University, Saudi Arabia, for supporting this work through project number (TU-DSPP-2024-06).

FUNDING

This research was funded by Taif University, Saudi Arabia, Project No. (TU-DSPP-2024-06).

REFERENCES

1. Alsuhaibani, A.M.; AlShawi, A.H.; Gaber, A.; Shakya, S.; Refat, M.S. A theoretical study on a new drug combines between vanadyl sulfate and vitamin E in a single component: A novel antioxidant medication in female reproductive health. *Bull. Chem. Soc. Ethiop*. **2024**, 38, 989-1001.
2. Shakya, B.; Shakya, S.; Hasan Siddique, Y. Effect of geraniol against arecoline induced toxicity in the third instar larvae of transgenic Drosophila melanogaster (hsp70-lacZ) Bg9. *Toxicol. Mech. Methods* **2019**, 29, 187-202.
3. Dai, Y.; Grant, S. Cyclin-dependent kinase inhibitors. *Curr Opin Pharmacol*. **2003**, 3, 362-370.
4. Huwe, A.; Mazitschek, R.; Giannis, A. Small molecules as inhibitors of cyclin-dependent kinases. *Angew. Chem. Int. Ed.* **2003**, 42, 2122-2138.
5. Been, M. D.; Champoux, J. J. Breakage of single-stranded DNA by eukaryotic type 1 topoisomerase occurs only at regions with the potential for base-pairing. *J. Mol. Biol.* **1984**, 180(3), 515-531.
6. Pommier, Y. Diversity of DNA topoisomerases I and inhibitors. *Biochimie* **1998**, 80, 255-270.
7. Huang, Z. Bcl-2 family proteins as targets for anticancer drug design. *Oncogene* **2000**, 19, 6627-6631.
8. Strawn, L.M.; McMahon, G.; App, H.; Schreck, R.; Kuchler, W.R.; Longhi, M.P.; Hui, T.H.; Tang, C.; Levitzki, A.; Gazit, A.; Chen, I.; Keri, G.; Orfi, L.; Risau, W.; Flamme, I.; Ullrich, A.; Hirth, K.P.; Shawver, L.K. Flk-1 as a target for tumor growth inhibition. *Cancer Res.* **1996**, 56, 3540-3545.
9. Al-Hazmi, G. H.; Hassanien, A. M.; Atta, A. A.; Refat, M. S.; Saad, H. A; Shakya, S.; Adam, A. M. A. Supramolecular charge-transfer complex generated by the interaction between tin

(II) 2, 3-naphtalocyanine as a donor with DDQ as an acceptor: Spectroscopic studies in solution state and theoretical calculations. *J. Mol. Liq.* **2022**, 362, 119757-119773.
10. Shi, Y.; Zou, Y.; Khan, M.S.; Zhang, M.; Yan, J.; Zheng, X.; Wang, W.; Xie, Z. Metal–organic framework-derived photoelectrochemical sensors: Structural design and biosensing technology. *J. Mater. Chem. C* **2023**, 11, 3692-3709.
11. Khan, M.S.; Hayat, M.U.; Khanam, M.; Saeed, H.; Owais, M.; Khalid, M.; Shahid, M.; Ahmad, M. Role of biologically important imidazole moiety on the antimicrobial and anticancer activity of Fe(III) and Mn(II) complexes. *J. Biomol. Struct. Dyn.* **2021**, 39, 4037-4050.
12. Zeng, Y.; Xu, G.; Kong, X.; Ye, G.; Guo, J.; Lu, C.; Nezamzadeh-Ejhieh, A.; Khan, M.S.; Liu, J.; Peng, Y. Recent advances of the core–shell MOFs in tumour therapy. *Int. J. Pharm.,* **2022**, 627, 122228-122250.
13. Zhang, W.; Ye, G.; Liao, D.; Chen, X.; Lu, C.; Nezamzadeh-Ejhieh, A.; Khan, M.S.; Liu, J.; Pan, Y.; Dai, Z. Recent advances of silver-based coordination polymers on antibacterial applications. *Molecules* **2022**, 27, 7166-7139.
14. Chen, J.; Cheng, F.; Luo, D.; Huang, J.; Ouyang, J.; Nezamzadeh-Ejhieh, A.; Khan, M.S.; Liu, J.; Peng, Y. Recent advances in Ti-based MOFs in biomedical applications. *Dalton Trans.* **2022**, 51, 14817-14832.
15. O'Boyle, N.M.; Banck, M.; James, C.A.; Morley, C.; Vandermeersch, T.; Hutchison, G.R.; Open Babel: An open chemical toolbox. *J. Cheminform.* **2011**, 3, 33-47.
16. Dallakyan, S. PyRx-python prescription v. 0.8.*The Scripps Research Institute*, 2008. **2010**.
17. Chu, C.H.; Li, K.M.; Lin, S.W.; Chang, M.D.T.; Jiang, T.Y.; Sun, Y.J. Crystal structures of starch binding domain from *Rhizopus oryzae* glucoamylase in complex with isomaltooligosaccharide: Insights into polysaccharide binding mechanism of CBM21 family. *Proteins: Struct. Funct., Bioinf.* **2014**, 82, 1079-1085.
18. Rehman, M.T.; AlAjmi, M.F.; Hussain, A. Natural compounds as inhibitors of SARS-CoV-2 main protease (3CLpro): A molecular docking and simulation approach to combat COVID-19. *Curr. Pharm. Des.* **2021**, 27, 3577-3589.
19. Trott, O.; Olson, A.J. AutoDock Vina: improving the speed and accuracy of docking with a new scoring function, efficient optimization, and multithreading. *J Comput Chem.* **2010**. 31, 455-461.
20. Shakya, S.; Khan, I.M.; Shakya, B.; Siddique, Y.H.; Varshney, H.; Jyoti, S. Protective effect of the newly synthesized and characterized charge transfer (CT) complex against arecoline induced toxicity in third-instar larvae of transgenic *Drosophila melanogaster* (hsp70-lacZ) Bg 9: Experimental and theoretical mechanistic insights. *J. Mat. Chem. B* **2023**, 11, 1262-1278.
21. Frisch, M.J.; Trucks, G.W.; Schlegel, H.B.; Scuseria, G.E.; Robb, M.A.; Cheeseman, J.R.; Scalmani, G.; Barone, V.; Petersson, G.A.; Nakatsuji, H.; Li, X.; Caricato, M.; Marenich, A.V.; Bloino, J.; Janesko, B.G.; Gomperts, R.; Mennucci, B.; Hratchian, H.P.; Ortiz, J.V.; Izmaylov, A.F.; Sonnenberg, J.L.; Williams-Young, D.; Ding, F.; Lipparini, F.; Egidi, F.; Goings, J.; Peng, B.; Petrone, A.; Henderson, T.; Ranasinghe, D.; Zakrzewski, V.G.; Gao, J.; Rega, N.; Zheng, G.; Liang, W.; Hada, M.; Ehara, M.; Toyota, K.; Fukuda, R.; Hasegawa, J.; Ishida, M.; Nakajima, T.; Honda, Y.; Kitao, O.; Nakai, H.; Vreven, T.; Throssell, K.; Montgomery, J.A., Jr.; Peralta, J.E.; Ogliaro, F.; Bearpark, M.J.; Heyd, J.J.; Brothers, E.N.; Kudin, K.N.; Staroverov, V.N.; Keith, T.A.; Kobayashi, R.; Normand, J.; Raghavachari, K.; Rendell, A.P.; Burant, J.C.; Iyengar, S.S.; Tomasi, J.; Cossi, M.; Millam, J.M.; Klene, M.; Adamo, C.; Cammi, R.; Ochterski, J. W.; Martin, R.L.; Morokuma, K.; Farkas, O.; Foresman, J.B.; Fox, D.J. *Gaussian 09*, Gaussian, Inc.: Wallingford CT; **2009**.
22. Salih, R.H.H.; Hasan, A.H.; Hussein, A.J.; Samad, M.K.; Shakya, S.; Jamalis, J.; Hawaiz, F.E.; Pratama, M.R.F. One-pot synthesis, molecular docking, ADMET, and DFT studies of novel pyrazolines as promising SARS-CoV-2 main protease inhibitors. *Rev. Chem. Intermed.* **2022**, 48, 4729-4751.

23. Hariharan, P.C.; Pople, J.A. The effect of d-functions on molecular orbital energies for hydrocarbons. *Chem. Phys. Lett.* **1972**, 16, 217-219.
24. Zhurko G.A.; Zhurko D.A. Chemcraft - graphical program for visualization of quantum chemistry computations. Ivanovo, Russia, Academic version 1.5. **2004**.
25. Hasan, A.H.; Yusof, F.S.; Kamarudin, N.A.; Murugesan, S.; Shakya, S.; Jamalis, J. Synthesis, anti-acetylcholinesterase evaluation, molecular docking and molecular dynamics simulation of novel Psoralen derivatives. *Curr. Org. Synth.* **2024**, 21, 61-77.
26. Alamri, A.S.; Alhomrani, M.; Alsanie, W.F.; Alyami, H.; Shakya, S.; Habeeballah, H.; Abdulaziz, O.; Alamri, A.; Alkhatabi, H.A.; Felimban, R.I.; Alhabeeb, A.A.; Refat, M.S.; Gaber, A. Spectroscopic and molecular docking analysis of π-acceptor complexes with the drug barbital. *Appl. Sci.* **2022**, 12, 10130.
27. Akram, M.; Lal, H.; Shakya, S.; Kabir-ud-Din. Multispectroscopic and computational analysis insight into the interaction of cationic diester-bonded gemini surfactants with serine protease α-chymotrypsin. *ACS Omega* **2020**, 5, 3624-3637.
28. Khan, I.M.; Shakya, S.; Islam, M.; Khan, S.; Najnin, H. Synthesis and spectrophotometric studies of CT complex between 1,2-dimethylimidazole and picric acid in different polar solvents: exploring antimicrobial activities and molecular (DNA) docking. *Phys. Chem. Liq.* **2021**, 59, 753-769.
29. Khan, I.M.; Islam, M.; Shakya, S.; Alam, N.; Imtiaz, S.; Islam, M.R. Synthesis, spectroscopic characterization, antimicrobial activity, molecular docking and DFT studies of proton transfer (H-bonded) complex of 8-aminoquinoline (donor) with chloranilic acid (acceptor). *J. Biomol. Struct. Dyn.* **2022**, 40, 12194-12208.
30. Ranjbar, A.; Jamshidi, M.; Torabi, S. Molecular modelling of the antiviral action of Resveratrol derivatives against the activity of two novel SARS CoV-2 and 2019-nCoV receptors. *Eur. Rev. Med. Pharmacol. Sci. Sci.* **2020**, 24, 7834-7844.
31. Alkathiri, A.A.; Atta, A.A.; Refat, M.S.; Shakya, S.; Hassanien, A.M.; Algarni, S.A.; Ahmed, E.M.; Alomariy, S.E.; Alsawat, M.; Algethami, N. Impedance spectroscopy and DFT/TD-DFT studies of diyttrium trioxide for optoelectronic fields. *J. Rare Earths.* **2023**, 41, 605-612.
32. Khan, I.M.; Naaz, F.; Shakya, S.; Islam, M.; Khan, A.; Ahmad, M. Photocatalytic activity, DFT/TD-DFT, and spectrophotometric studies of a synthesized charge transfer complex of *p*-toluidine with 1,2,4,5-benzenetetracarboxylic acid in various polar solvents. *J. Mol. Liq.* **2024**, 399, 124412-124426.
33. Al-Hazmi, G.H.; Ibrahim, A.A.; Refat, M.S.; Adam, F.A.; Allam, A.; Shakya, S.; Alsuhaibani, A.M. Intermolecular charge-transfer complexes between chlorothiazide antihypertensive drug against iodine sigma and picric acid pi acceptors: DFT and molecular docking interaction study with Covid-19 protease. *J. Indian Chem. Soc.* **2022**, 99, 100605.
34. Shakya, S.; Khan, I.M.; Ahmad, M. Charge transfer complex based real-time colorimetric chemosensor for rapid recognition of dinitrobenzene and discriminative detection of Fe^{2+} ions in aqueous media and human hemoglobin. *J. Photochem. Photobiol. A Chem.* **2020**, 392, 112402-112415.
35. Islam, M.R.; Shakya, S.; Selim, A.; Alam, M.S.; Ali, M. Solvatochromic absorbance and fluorescence probe behavior within ionic liquid+ γ-butyrolactone mixture. *J. Chem. amp; Eng. Data* **2019**, 64, 4169-4180.
36. Yu, W.; He, X.; Vanommeslaeghe, K.; MacKerell, A.D., Jr. Extension of the CHARMM General Force Field to sulfonylcontaining compounds and its utility in biomolecular simulations. *J. Comput. Chem.* **2012**, 33, 2451-2468.
37. Abraham, M.J.; Murtola, T.; Schulz, R.; Páll, S.; Smith, J.C.; Hess, B.; Lindahl, E. GROMACS: High performance molecular simulations through multi-level parallelism from laptops to supercomputers. SoftwareX, **2015**, 1, 19-25.
38. Murugavel, S.; Ravikumar, C.; Jaabil, G.; Alagusundaram, P. Synthesis, crystal structure analysis, spectral investigations (NMR, FT-IR, UV), DFT calculations, ADMET studies,

molecular docking and anticancer activity of 2-(1-benzyl-5-methyl-1H-1,2,3-triazol-4-yl)-4-(2-chlorophenyl)-6-methoxypyridine–a novel potent human topoisomerase IIα inhibitor. *J. Mol. Struct.* **2019**, 1176, 729-742.
39. Khan, I.M.; Shakya, S. Exploring colorimetric real-time sensing behavior of a newly designed CT complex toward nitrobenzene and Co^{2+}: Spectrophotometric, DFT/BarCS-DFT, and mechanistic insights. *ACS Omega* **2019**, 4, 9983-9995.
40. Refat, M.S.; Gaber, A.; Althobaiti, Y.S.; Alyami, H.; Alsanie, W.F.; Shakya, S.; Adam, A.M.A.; Kobeasy, M.I.; Asla, K.A. Spectroscopic and molecular docking studies of Cu(II), Ni(II), Co(II), and Mn(II) complexes with anticonvulsant therapeutic agent gabapentin. *Molecules.* **2022**, 27, 4311-4330.
41. Alkathiri, A.A.; Atta, A.A.; Refat, M.S.; Altalhi, T.A.; Shakya, S.; Alsawat, M.; Adam, A.M.A.; Mersal, G.A.; Hassanien, A.M. Preparation, spectroscopic, cyclic voltammetry and DFT/TD-DFT studies on fluorescein charge transfer complex for photonic applications. *Bull. Chem. Soc. Ethiop.* **2023**, 37, 515-532.